



Mathematical model for silicon electrode – Part I. 2-d model



Godfrey Sikha^{a,*}, Sumitava De^b, Joseph Gordon^a

^a Applied Materials Inc., 3225 Oakmead Village Drive, Santa Clara, CA 95054, USA

^b Department of Energy, Environmental and Chemical Engineering, Washington University, St. Louis, MO 63130, USA

HIGHLIGHTS

- A 2-d transient mathematical model to simulate the electrochemical lithiation in silicon nano-wire structure is developed.
- The model geometry is an axisymmetric cylindrical silicon nanowire electrode anchored to a copper current collector substrate.
- Model physics include diffusive transport of lithium, volume expansion, and diffusion induced stresses.
- Larger radius of the nanowire, and faster lithiation rates lead to increased radial and tangential stresses in the nanowire.

ARTICLE INFO

Article history:

Received 17 February 2014

Accepted 8 March 2014

Available online 21 March 2014

Keywords:

Li-ion battery

Silicon anodes

Intercalation induced stress generation

Mathematical model

ABSTRACT

This paper presents a 2-dimensional transient numerical model to simulate the electrochemical lithium insertion in a silicon nanowire (Si NW) electrode. The model geometry is a cylindrical Si NW electrode anchored to a copper current collector (Cu CC) substrate. The model solves for diffusion of lithium in Si NW, stress generation in the Si NW due to chemical and elastic strains, stress generation in the Cu CC due to elastic strain, and volume expansion in the Si NW and Cu CC geometries. The evolution of stress components, i.e., radial, axial and tangential stresses in different regions in the Si NW are presented and discussed. The effect of radius of Si NW and lithiation rate, on the maximum stresses developed in the Si NW are also discussed.

© 2014 Elsevier B.V. All rights reserved.

1. Introduction

Silicon electrode is pursued as a potential negative electrode for lithium-ion batteries owing to its high gravimetric (mAh g^{-1}) and volumetric capacity (mAh L^{-1}) compared to the existing state of the art graphite electrode [1]. One of the critical challenges in the commercialization of Si electrode is to minimize particle fracture developed during lithiation and delithiation of the Si electrode [2,3]. Recent experimental studies have demonstrated the use of nano-size Si structures as electrodes. These electrode structures exhibited minimal particle fracture and also enabled repeated cycling [4–6]. While different mechanisms have been proposed for this behavior, a detailed physics based analysis combining the electrochemical and structural aspects of lithium insertion in such nanostructures have not been undertaken. A variety of detailed phenomenological models exists in the literature for lithium intercalation in porous electrodes, which treat the transport of

electrolyte due to diffusion and migration, reaction kinetics at interfaces, and transport of Li and electrons in solid phase [7–13]. The general modeling framework presented in these papers cannot be directly used to simulate advanced high capacity electrodes, specifically the alloy type electrodes such as Si, Sn etc., because (a) the stresses developed during lithium insertion/deinsertion and (b) volume change associated with lithium insertion/deinsertion are not considered. So to accurately model such type of high capacity electrodes which undergo substantial volume changes, particle level expansion/contraction and electrode level displacement along with build up of stresses have to be captured. Early research by Prussin [14] demonstrated that the diffusion induced stresses generated by concentration distributions are of similar nature to the thermal stresses developed in an elastic medium. Modeling of diffusion induced stresses was also studied in detail by other researchers [15–18] for different geometries such as hollow cylinders, plates etc. Similar approaches were extended to battery electrode chemistries on a particle level to calculate intercalation induced stresses assuming no volume changes. Zhang et al. [19] presented a numerical model to calculate diffusion induced stresses for spherical and ellipsoidal shaped LiMn_2O_4 single particle. Also, the work by Cheng and Verbrugge [20,21] derived analytical expressions

DOI of original article: <http://dx.doi.org/10.1016/j.jpowsour.2014.03.130>.

* Corresponding author.

E-mail addresses: Godfrey_Sikha@amat.com, Sikha.Godfrey@gmail.com (G. Sikha).

(assuming negligible pressure induced diffusion and no volume change) to calculate stresses that arise from concentration gradients for a spherical particle. This modeling framework was also incorporated into a porous electrode framework [22]. All the above referenced models in addition to other published work [23–25] were developed assuming dilute solution theory for diffusion within particle, with no moving boundaries (negligible volume change) and for low expansion materials.

Christensen et al. [26] presented a more rigorous mathematical framework based on concentrated solution theory, which incorporates volume expansion and stress build up in a single spherical particle electrode and case studies for lithiation in a spherical carbon particle (8% volume expansion) were discussed. The same framework was also used to calculate the stresses in LiMn_2O_4 single spherical particle electrode [27] and was also later extended to porous electrodes [28] containing graphitic mesophase-carbon-microbead (MCMC) anode and lithium manganese oxide spinel cathode. The author also emphasizes the importance of thermodynamic factor, pressure driven diffusion and extent of volume change in determining the cell potential profiles and initiation of fracture. However most of the above mentioned work was based on electrodes which undergo volume change in the order of 10%. To model large volume expansion in electrodes, Chandrasekaran et al. [29] modeled a single particle Si electrode under galvanostatic and potentiodynamic control of lithiation of Si to $\text{Li}_{3.75}\text{Si}$ associated with a 270% volume change. In a later paper [30], the same approach was extended to a porous electrode to describe how particle level expansion affects the porosity of the electrode. The authors ignored stress calculations based on the assumption that the nano sized particles would not build appreciable concentration gradients to generate diffusion induced stresses. Gao et al. [31] modeled stress build up due to concentration gradients for a 1-d (radial) cylindrical geometry for a nano sized Si electrode for a dilute solid solution with constant density. The authors also discuss the strong coupling between stress enhanced diffusion and diffusion induced stresses for electrodes associated with large volume expansion.

In this paper (Part I), we present a model to describe diffusion and stress build up in a 2-d silicon nanowire (Si NW) geometry

anchored to a Cu substrate under galvanostatic conditions. The model in general follows the framework described in reference [26] but applied to Si electrode with a maximum lithiation to $\text{Li}_{3.75}\text{Si}$ associated with a 270% volume change. Case studies related to lithiation rate & nanowire radius are presented. In the second part of the paper (Part II), a dimensionally reduced 1-d model (in the radial co-ordinate) is presented and the predictions between the 1-d and 2-d model are compared. The concentration and stress profiles predicted by the 1-d model compares well with the 2-d model at regions far away from the Cu substrate. Consequently, the 1-d model was used to analyze different geometries - nanotube & core/shell structures and the evolution of stresses in these geometries are compared to the nanowire geometry.

2. Model development

2.1. Assumptions

The geometry of the Si NW anchored to the Cu CC substrate is shown in Fig. 1 (left); the initial unexpanded radius and the length of the Si NW are $R_{\text{NW}} = 50 \text{ nm}$ and $H_{\text{NW}} = 10 \mu$ respectively. The model geometry consists of a 2-d axisymmetric cut from the overall geometry as shown in Fig. 1 (right), wherein the dependence of the variables in the θ direction was ignored. Other key assumptions in the model were

- The charge storage mechanism in the Si electrode is modeled by considering the electrochemical reaction of Li at the surface of the Si NW followed by transport of Li into the Si NW. The lithiated Si mixture is represented as a solid solution, therefore phase transitions are ignored.
- The transport of the host silicon is solely due to the convective flux, where as the transport of lithium is due to the combined effect of gradients in concentration and pressure, and convective flux.
- Lithium diffusion into Cu CC substrate is ignored and therefore the Si NW/Cu CC interface acts as a Li blocking interface.
- Stress strain relationship was assumed to obey Hooke's law (linear) in the entire lithiation regime. For particles of nanometer radii, the stress generated due to insertion is typically less

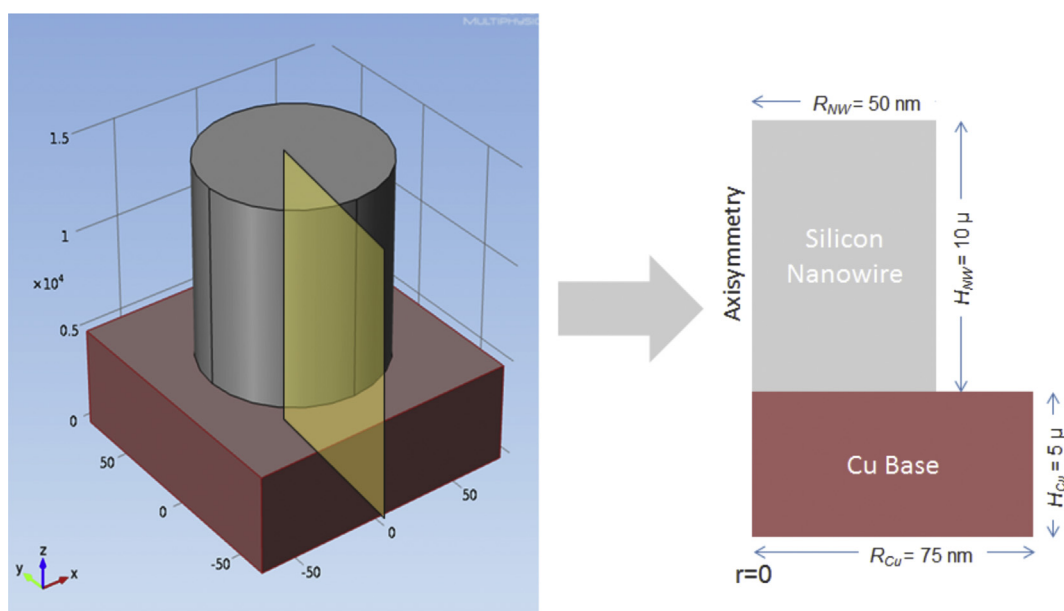


Fig. 1. Schematic of the Si NW anchored to the Cu CC substrate (left). 2-d axisymmetric slice of Si NW anchored to Cu CC base substrate used as the geometry for the 2-d model (right).

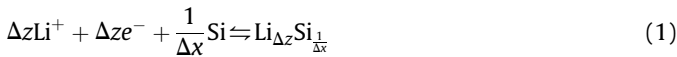
than the yield stress limit for onset of plasticity, therefore the system is assumed to stay elastic throughout lithiation.

- For galvanostatic studies, the total current to the Si NW was maintained constant; the current density at the surface of the Si NW was taken to be constant spatially, however it changes with time in accordance with the increase in surface area related to volume expansion.
- Isothermal conditions were assumed during lithiation of the Si NW.

2.2. Model equations

2.2.1. Material balance

The electrochemical equilibrium reaction between Li and Si is written in the form



The above reaction can be thought of a single electron transfer reaction ($\text{Li}^+ + e^- \rightleftharpoons \text{Li}$), followed by lithium alloying with $\text{Si}_{1/\Delta x}$, where Δz (varies between 0 and 1) is the insertion coefficient of Li in $\text{Li}_{\Delta z} \text{Si}_{1/\Delta x}$ and Δx is the maximum number of moles of Li that can reversibly alloy with Si. The value of Δx was measured to be 22/5 in earlier work [32] at high temperatures, however at room temperatures with electrochemical lithiation, the value of Δx was measured to be 15/4 by different groups [33–35]. In our work, the value for Δx was taken to be 15/4. Based on the earlier work [26], the binary species chosen are the empty (Li free) host lattice and the lithiated host lattice. Note, the host lattice in this work is $1/\Delta x \text{Si}$ and the lithiated host is $\text{LiSi}_{1/\Delta x}$ and will be denoted hereafter as S and LiS respectively.

In the Si NW electrode, the flux of LiS is obtained through the generalized Maxwell–Stefan equation [36]. Considering ideal solution, ignoring thermal and external forced diffusion effects in the generalized Maxwell–Stefan relation and rearranging for the flux of species N_{LiS} we obtain

$$N_{\text{LiS}} = x_{\text{LiS}}(N_{\text{LiS}} + N_{\text{S}}) - c_T D_{\text{LiS,S}} \left[\alpha_{\text{LiS}} \nabla x_{\text{LiS}} + \frac{x_{\text{LiS}}}{RT} \left(\tilde{V}_{\text{LiS}} - \frac{M_{\text{LiS}}}{\rho} \right) \nabla p \right] \quad (2)$$

where N_{LiS} , N_{S} and x_{LiS} , x_{S} are the molar fluxes and mole fractions of the respective species, M_{LiS} and \tilde{V}_{LiS} are the molar mass and molar volume of LiS, c_T is the total concentration, i.e. $c_T = c_{\text{LiS}} + c_{\text{S}}$, α_{LiS} is the thermodynamic factor and ρ is the density of the material

$$\rho = c_T \sum x_i M_i \quad (3)$$

The flux of S is considered purely to be convective, and the lattice velocity is defined through the molar averaged velocity, i.e. $v^\diamond = x_{\text{LiS}} v_{\text{LiS}} + x_{\text{S}} v_{\text{S}}$. The total molar flux is related to the molar average velocity as

$$N_{\text{LiS}} + N_{\text{S}} = c_T v^\diamond \quad (4)$$

The partial molar volume of species LiS, \tilde{V}_{LiS} is given as a function of the molar volume of the host material \tilde{V}_{S} and the expansion factor ξ , where ξ can be considered as an experimentally measured parameter defined as the percentage volume change expressed in fraction, at a particular value of Δz .

$$\tilde{V}_{\text{LiS}} = \tilde{V}_{\text{S}} \left(1 + \frac{\xi}{\Delta z} \right) \quad (5)$$

where Δz is the insertion coefficient of Li in $\text{Li}_{\Delta z} \text{Si}_{1/\Delta x}$. The mass balance for the species LiS is written as

$$\frac{\partial(c_T x_{\text{LiS}})}{\partial t} + \nabla \cdot N_{\text{LiS}} = 0 \quad (6)$$

The total concentration, c_T and the pressure p will be described after discussion of the diffusion induced stresses.

At the outer boundary of the Si NW, a constant current flux condition was used as the boundary condition, while at the center an axial symmetry condition was used. In a strict sense, the electrode kinetics and the mass transfer of the species in solution could determine the actual current distribution at the electrode surface, however in this study, we have restricted our simulations for the case of uniform current distribution along the nanowire.

$$\begin{cases} -n \cdot N_{\text{LiS}}|_{r=R_{\text{NW}}(t),z} = \frac{-S_i i_{\text{app}}(t)}{F} \\ -n \cdot N_{\text{LiS}}|_{r,z=H_{\text{NW}}(t)} = \frac{-S_i i_{\text{app}}(t)}{F} \end{cases} \quad (7)$$

$$-n \cdot N_{\text{LiS}}|_{r=0,z} = 0 \quad (8)$$

where $i_{\text{app}}(t)$ is the current normalized to the external surface area of the Si NW.

2.2.2. Force balance

The strain for the case of small deformation is generally described in the tensor notation as

$$\epsilon = \frac{1}{2} (\mathbf{u} \nabla_{\mathbf{x}} + (\mathbf{u} \nabla_{\mathbf{x}})^T) \quad (9)$$

For large deformation analysis, the Lagrangian strain (Green strain) is related to the displacement gradient as follows:

$$\epsilon = \frac{1}{2} (\mathbf{u} \nabla_{\mathbf{x}} + \nabla_{\mathbf{x}} \mathbf{u} - \mathbf{u} \nabla_{\mathbf{x}} (\mathbf{u} \nabla_{\mathbf{x}})^T) \quad (10)$$

where \mathbf{u} is the displacement vector calculated from the current and the initial configuration of the volume element. For finite deformation, the strain tensor for the 2-d axial symmetry case, in the cylindrical co-ordinates is written as

$$\epsilon = \begin{bmatrix} \epsilon_{rr} & \epsilon_{r\theta} & \epsilon_{rz} \\ \epsilon_{\theta r} & \epsilon_{\theta\theta} & \epsilon_{\theta z} \\ \epsilon_{zr} & \epsilon_{z\theta} & \epsilon_{zz} \end{bmatrix} = \begin{bmatrix} \frac{\partial u}{\partial r} + \frac{1}{2} \left[\left(\frac{\partial u}{\partial r} \right)^2 + \left(\frac{\partial w}{\partial r} \right)^2 \right] & 0 & \frac{1}{2} \left(\frac{\partial u}{\partial z} + \frac{\partial w}{\partial r} + \frac{\partial u}{\partial r} \frac{\partial u}{\partial z} + \frac{\partial w}{\partial r} \frac{\partial w}{\partial z} \right) \\ 0 & \frac{u}{r} + \frac{1}{2} \left(\frac{u}{r} \right)^2 & 0 \\ 0 & 0 & \frac{\partial w}{\partial z} + \frac{1}{2} \left[\left(\frac{\partial u}{\partial z} \right)^2 + \left(\frac{\partial w}{\partial z} \right)^2 \right] \end{bmatrix} \quad (11)$$

where u, v, w are the displacements corresponding to elastic strains, in the r, θ , and z directions respectively. The displacement v in the θ direction is zero based on the axisymmetry assumption; subsequently $\epsilon_{r\theta}$ and $\epsilon_{\theta z}$ are also zero. The symmetric stress tensor describes the stress components in the material and contains three normal stress $\sigma_{rr}, \sigma_{\theta\theta}, \sigma_{zz}$ and the three symmetric shear stresses, i.e. $\tau_{r\theta}, \tau_{\theta z}, \tau_{rz}$ and the components are given as

$$\boldsymbol{\tau} = \begin{bmatrix} \sigma_{rr} & \tau_{r\theta} & \tau_{rz} \\ \tau_{\theta r} & \sigma_{\theta\theta} & \tau_{\theta z} \\ \tau_{zr} & \tau_{z\theta} & \sigma_{zz} \end{bmatrix} \begin{cases} \tau_{rz} = \tau_{zr} \\ \tau_{r\theta} = \tau_{\theta r} \\ \tau_{\theta z} = \tau_{z\theta} \end{cases} \quad (12)$$

The elastic stresses are correlated to the strains using the elastic moduli matrix, which is a fourth order tensor, because of the symmetry and isotropic assumption, the number of independent parameters in this matrix is reduced to 2, i.e. the Lamé parameters, λ and μ . The stress–strain relationship therefore reduces to

$$\boldsymbol{\tau} = \lambda \text{tr}(\boldsymbol{\epsilon})(\mathbf{I}) + 2\mu(\boldsymbol{\epsilon}) \quad (13)$$

The Lamé parameters could be related to the more commonly used material properties, Young's modulus (E) and Poisson's ratio (ν) through the relations.

$$E = \frac{(3\lambda + 2\mu)\mu}{\lambda + \mu}, \quad \nu = \frac{\lambda}{2(\lambda + \mu)} \quad (14)$$

In this system, the insertion of Li into the Si host introduces a significant volume change, atypical of common insertion electrodes such as LiMn_2O_4 , LiCoO_2 , $\text{LiTi}_5\text{O}_{12}$ etc., where the total volume change is typically less than 10% and therefore ignored in most models. To include the volume change formalism into the modeling framework, the total strain in the electrode is defined as the summation of the two components, chemical strain (stress free) and elastic strain, i.e., $\epsilon_T = \epsilon_{ch} + \epsilon_{el}$; and the chemical strain is expressed as a function of the partial molar volumes and mole fractions of the species LiS and S , (note $x_{\text{LiS}} + x_{\text{S}} = 1$):

$$\epsilon_{ch} = \frac{x_{\text{LiS}}}{3} \left(\frac{\tilde{V}_{\text{LiS}}}{\tilde{V}_{\text{S}}} - 1 \right) (\mathbf{I}) \quad (15)$$

Consequently, the elastic strain can be written as the difference between the total strain and the chemical strain, which can be substituted back into equation (12) to obtain the stress–strain relationship for electrodes undergoing elastic and chemical strains.

$$\boldsymbol{\epsilon} = \boldsymbol{\epsilon}_T - \boldsymbol{\epsilon}_{ch} \quad (16)$$

The total concentration c_T as described in equation (6) is written as a function of composition and pressure, which is related to the trace of the stress tensor

$$c_T = \xi(x_{\text{LiS}}, x_{\text{S}}) \psi(\text{tr}(\boldsymbol{\tau})) \quad (17)$$

The function ξ is purely composition dependent and can be defined as a function of partial molar volumes of the individual species. The function ψ is evaluated similar to the work of Christensen et al. [27] using the definition of a compressibility factor in terms of differential volume element and mean normal pressure. Subsequently, equation (17) is expressed as

$$c_T = (x_{\text{LiS}} \tilde{V}_{\text{LiS}} + x_{\text{S}} \tilde{V}_{\text{S}})^{-1} \exp \left[-\frac{1}{3K} \text{tr}(\boldsymbol{\tau}) \right] \quad (18)$$

where K is the bulk modulus of the material. The pressure defined in equation (2) is the thermodynamic pressure, which is assumed to be equivalent to the mean normal pressure, and is expressed as

$$p = -\frac{1}{3} \text{tr}(\boldsymbol{\tau}) \quad (19)$$

Finally, the equilibrium force balance equation in the 2-d axisymmetry geometry is expressed as

$$\frac{\partial \sigma_{rr}}{\partial r} + \frac{\partial \tau_{rz}}{\partial z} + \frac{\sigma_{rr} - \sigma_{\theta\theta}}{r} = 0 \quad (20)$$

$$\frac{\partial \tau_{rz}}{\partial r} + \frac{\partial \sigma_{zz}}{\partial z} + \frac{\tau_{rz}}{r} = 0 \quad (21)$$

The individual velocity components of \mathbf{v}^\diamond in equation (4) is calculated from the time derivatives of corresponding displacement fields.

$$v_r = \frac{\partial u}{\partial t} \Big|_{r,z} \quad (22)$$

$$v_z = \frac{\partial w}{\partial t} \Big|_{r,z} \quad (23)$$

Equations (6), (18), (20) and (21) were used to solve for the variables u, w, x_{LiS} , and c_T respectively in the Si NW domain. The equilibrium force balance equations (20) and (21) are also valid in the Cu CC domain, with the exception that the total strain, ϵ_T is purely elastic and the chemical strain component is absent based on the assumption that lithium does not transport into the Cu substrate. Therefore the displacement components u, w are the only variables to be solved for in the Cu CC domain.

The force balance equation in the Si NW was constrained to the following boundary conditions

$$\begin{cases} \sigma_{rr}|_{r=R_{\text{NW}}(t),z} = 0 \\ \sigma_{zz}|_{r,z=H_{\text{NW}}(t)} = 0 \end{cases} \quad (24)$$

The base of the Cu CC substrate is subjected to a fixed constraint boundary conditions

$$\begin{cases} u|_{r,z=0} = 0 \\ w|_{r,z=0} = 0 \end{cases} \quad (25)$$

The outer surface of the Si NW, the top unanchored portion of the Cu CC and the outer surface of the Cu CC are assumed to be free surfaces i.e.

$$-\mathbf{n} \cdot \boldsymbol{\tau} = 0 \quad (26)$$

3. Solving methodology & parameters

The equations are solved using COMSOL Multiphysics with the structural mechanics module to solve for the displacement components u, w equations (20) and (21) and a general PDE interface to solve for x_{LiS} equation (6). The mass balance equations were re-written in terms of material derivatives for the ease of implementation in the material framework in COMSOL.

Since the dimensions of the Si NW change significantly upon lithiation, the initial mesh configuration has to be updated at each time step to accommodate for the updated geometry. In this model, the deformation of the mesh is determined by the displacement components (u, w) calculated from structural mechanics module. The technique for mesh movement is called an Arbitrary Lagrangian–Eulerian (ALE) method, which is an intermediate between the Lagrangian and Eulerian methods, and it allows moving boundaries without the need for the mesh movement to follow the material. For the 2-d model, the Si NW part of the geometry was

Table 1
List of parameter values used in the simulation.

Parameter	Value	Units
Partial molar volume of LiS, \bar{V}_{LiS}	13.11	ml mol ⁻¹
Molar volume of S, \bar{V}_{S}	3.214	ml mol ⁻¹
Maximum number of moles of Li that can reversibly alloy per mole of Si, Δx	15/4	No units
Maximum insertion coefficient of Li in LiS, Δz_{max}	1	No units
Diffusion coefficient of Li in Si, $D_{\text{LiS,S}}$	2×10^{-12}	cm ² s ⁻¹
Young's modulus of LiS, E	92.16	GPa
Poisson's ratio of LiS, ν	0.27	No units
Young's modulus of Cu substrate, E_{Cu}	110	GPa
Poisson's ratio of Cu substrate, ν_{Cu}	0.35	No units
Thermodynamic factor, α	1	No units
Expansion fraction, ξ (measured at Δz_{max})	3.079	No units

mapped with 300 node points along the axial direction, and 100 points along the radius, while the base Cu CC structure was mapped with 150 node points along the axial direction and 150 node points along the radius. In all, the geometry consisted of 52,500 quadrilateral, 1300 line and 7 vertex elements. An absolute tolerance of 10^{-15} and 10^{-6} was used for the displacement variables (u , w) and x_{LiS} respectively, and a relative tolerance of 10^{-5} was used to establish convergence. Automatic time stepping (based on the solver) was used, and the computational run time taken for a complete charge (167 time steps) was 17281 s, using a 16 core Intel Xeon 2.27 GHz processor. The parameters used in the model are given in Table 1.

4. Results and discussion

4.1. Diffusion induced stresses

Fig. 2a shows the mole fraction distribution of LiS in the Si NW at the end of lithiation. The lithiation rate in this simulation

corresponds to a surface current density of 0.02 mA cm⁻²(initial) equivalent to a 1-h rate. The solid line in the plot marks the initial undeformed configuration of the Si NW anchored to the Cu CC substrate. In this study, the simulation was terminated when the local mole fraction reached, $x_{\text{LiS}} = 1$ anywhere within the electrode. As observed from the plot, the top surface of the Si NW is mass transfer limited and gets completely lithiated ($x_{\text{LiS}} = 1$) while the bulk of the Si NW is still partially lithiated ($x_{\text{LiS}} = 0.86$), which limits complete electrode utilization. The final deformed configuration of the Si NW shows the increase in the radial and axial dimensions of the Si NW due to the combination of chemical and elastic strains during lithiation. The top of the Si NW is expanded more, due to maximum lithiation in that region resulting in increased chemical strain, and regions very close to the Si NW/Cu CC interface (as shown in Fig. 2b) are minimally expanded as the lithiation is limited due to the high stresses developed at the lithium blocking interface. Fig. 2b also shows the displacement of the Si NW/Cu CC interface from the initial configuration due to the interfacial stresses. Note, the Si NW region is pushed into the Cu CC region (z axis) by ~ 1 nm.

Fig. 3 shows a snap shot of the local volumetric strain distribution in the structure at the end of lithiation. The volumetric strain in the Si NW is non-uniform in the axial direction, especially at the top and the Si NW/Cu CC interface regions. In general, the local volumetric strain distribution in the Si NW domain correlates to the concentration distribution in Fig. 2a, because the total volumetric strain, defined in equation (16) is predominantly determined by the chemical strain. In the Cu domain, the volumetric strains are purely elastic and mostly tensile, except at regions close to the Si NW/Cu CC and away from the center where some regions are compressive.

Fig. 4 compares the radial, tangential and axial stress components across the radius of the Si NW at different times during lithiation. The radial cut section in this plot is taken at half the initial height of the Si NW ($z = H_{\text{Cu}} + H_{\text{NW}}/2$). Several features are observed in this plot; firstly the radial stress across the radius of the

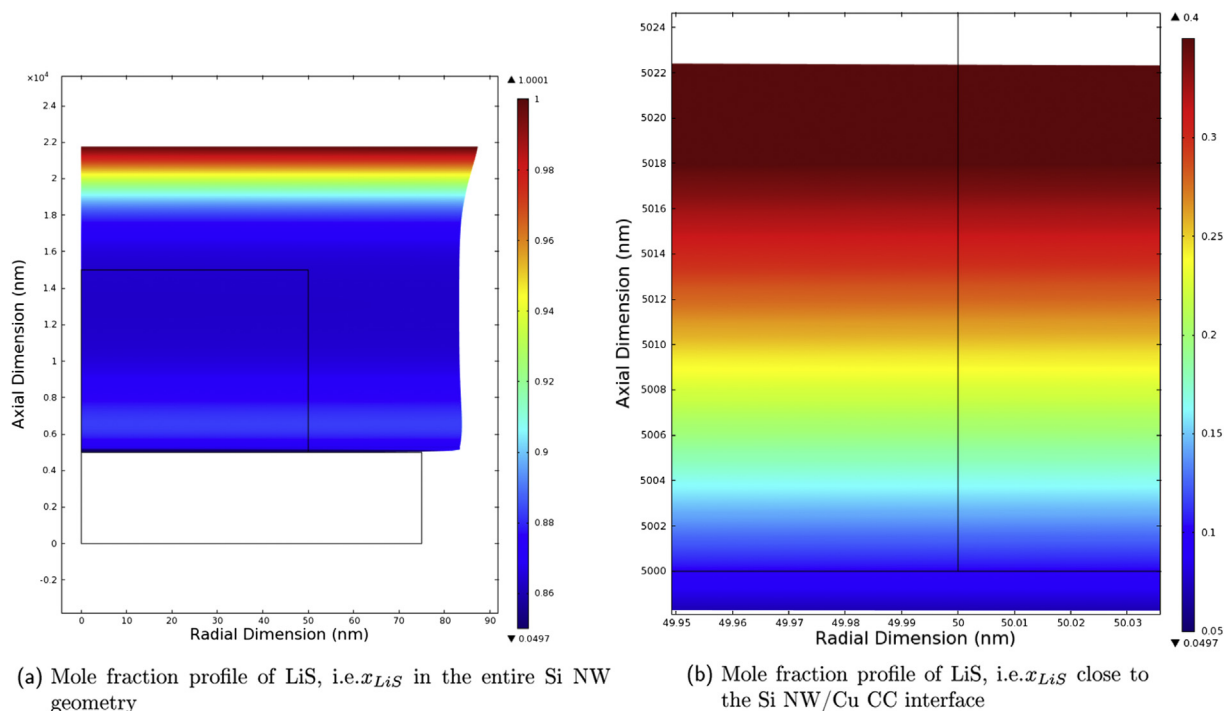


Fig. 2. Mole fraction distribution in the Si NW at end of lithiation. A constant 1-hr rate current equivalent to a current density (initial) of 0.0208 mA cm⁻² was used in this simulation.

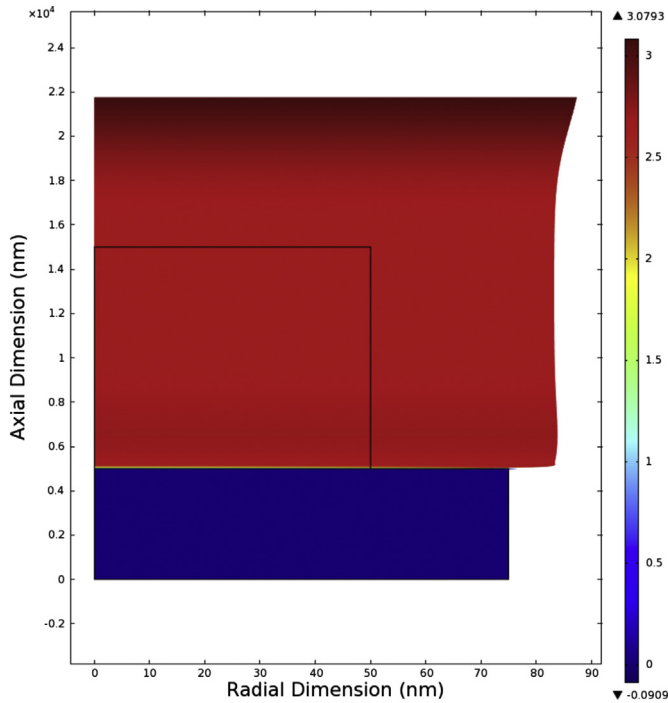


Fig. 3. Volumetric strain distribution in the Si NW/Cu CC at the end of lithiation. A constant 1-hr rate current equivalent to a current density (initial) of $0.0208 \text{ mA cm}^{-2}$ was used in this simulation.

Si NW is always tensile, and is maximum at the center. This is because of the concentration build up at the surface which causes volumetric strain in the outer layers, which in turn radially pulls the inner layers to create the tensile stresses throughout the radius of the Si NW (as plotted in Fig. 4a, b, c, & d). As a function of time, the maximum radial stresses (at the center of the Si NW) increase up to the first 10 s ($\sim 43 \text{ MPa}$ observed at 10 s) and continuously decrease at longer times ($\sim 2 \text{ MPa}$ observed at 1000 s). Also, the maximum tangential and the axial stresses follow a similar trend. This behavior is due to the competing effects of the chemical diffusion term and the pressure induced term in equation (2) towards the overall flux of the species. At short times, the species flux is dominated by the chemical diffusion term, while at longer times, is dominated by pressure gradient term, resulting in reduced concentration gradients. Since the build up of stresses is proportional to concentration gradients based on equation (16) and the force balance relations (equations (20) and (21)), the stresses decrease when the flux is dominated by the pressure gradients. Secondly, the tangential and the axial stresses are always compressive towards the outer surface and tensile towards the inner core. This behavior is due to the radial expansion of the outer surface which creates compressive strains in the tangential and the axial direction towards the outer surface, while the inner core is pulled outwards in all coordinates creating tensile stresses in the tangential and axial directions. Thirdly, at the center of the Si NW, the radial and the tangential stresses are equal, and the magnitude of the axial stress is twice the radial or tangential stress. This scenario is representative of a 1-d plane strain condition with infinitesimal deformation, where the condition $\sigma_{rr} = \sigma_{\theta\theta} = \sigma_{zz}/2$ is satisfied at the center ($r = 0$) in cylindrical coordinates. This behavior suggests that far

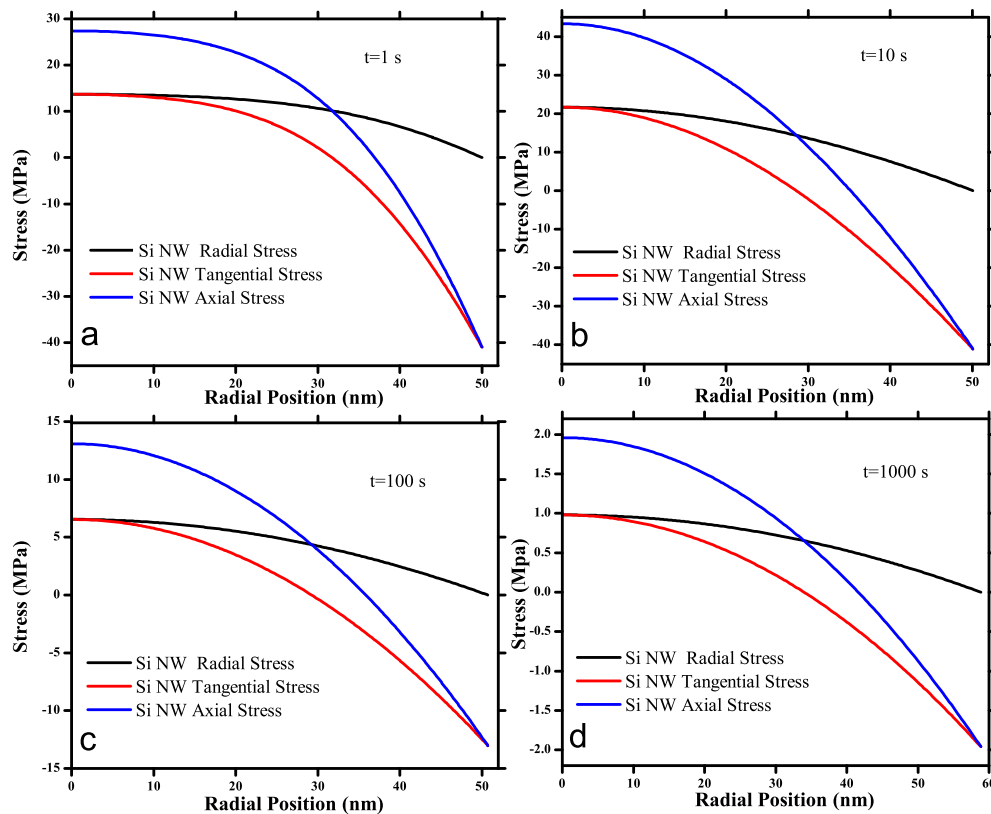


Fig. 4. Profiles of radial, tangential, and the axial stresses across the radius of the Si NW at half the height of the nanowire ($z = H_{\text{Cu}} + H_{\text{NW}}/2$) at various times: a) 1 s, b) 10 s, c) 100 s & d) 1000 s. A constant 1-hr rate current equivalent to a current density (initial) of $0.0208 \text{ mA cm}^{-2}$ was used in these simulations.

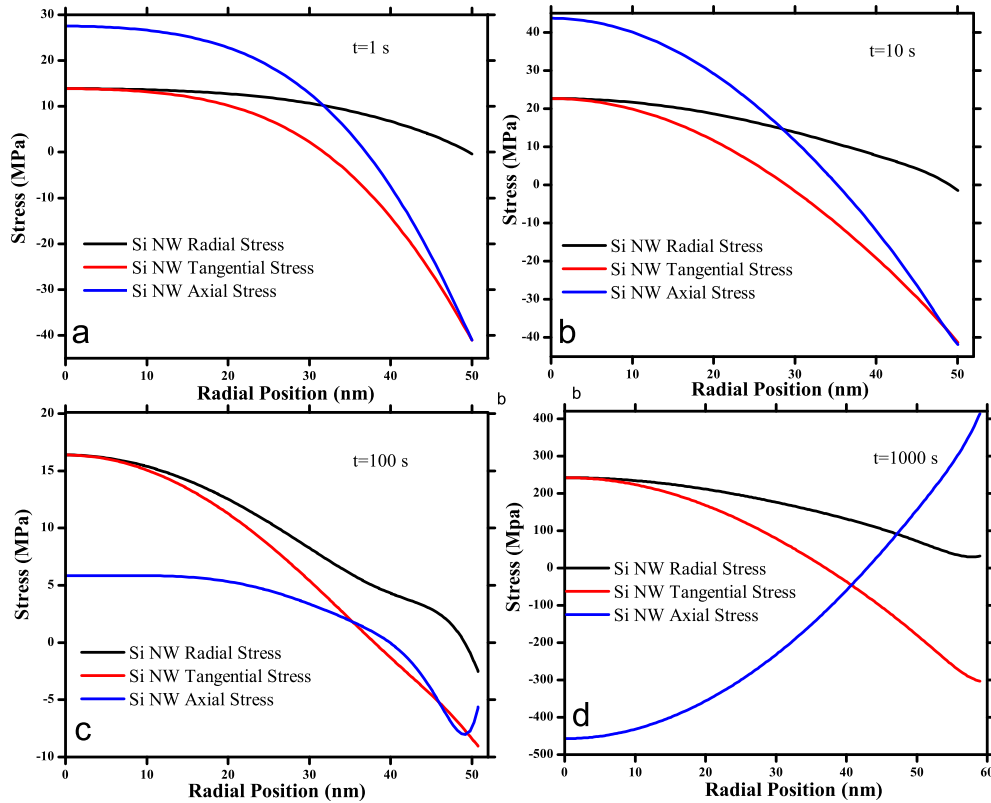


Fig. 5. Profiles of radial, tangential, and the axial stresses across the radius of the Si NW, close to the Si NW/Cu CC interface ($z = H_{Cu}$) at various times: a) 1 s, b) 10 s, c) 100 s & d) 1000 s. A constant 1-hr rate current equivalent to a current density (initial) of $0.0208 \text{ mA cm}^{-2}$ was used in these simulations.

away from the Si NW/Cu CC interface, the stress behavior is similar to a 1-d plane strain condition.

Fig. 5 compares the radial, tangential and axial stress components close to the Si NW/Cu CC interface on the Si NW side. At

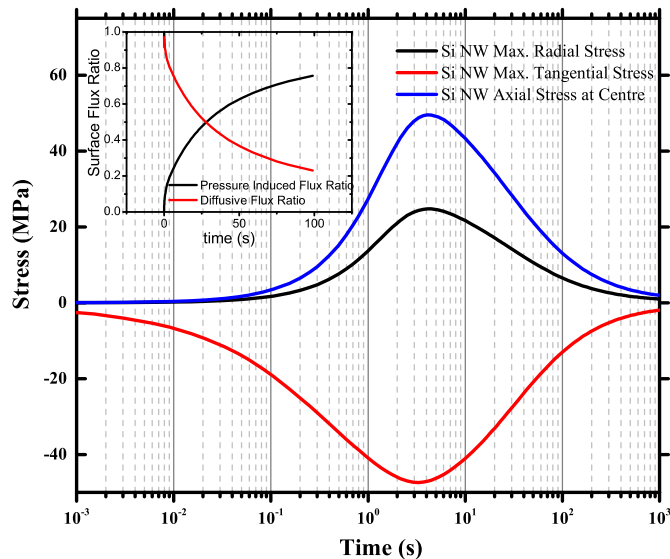
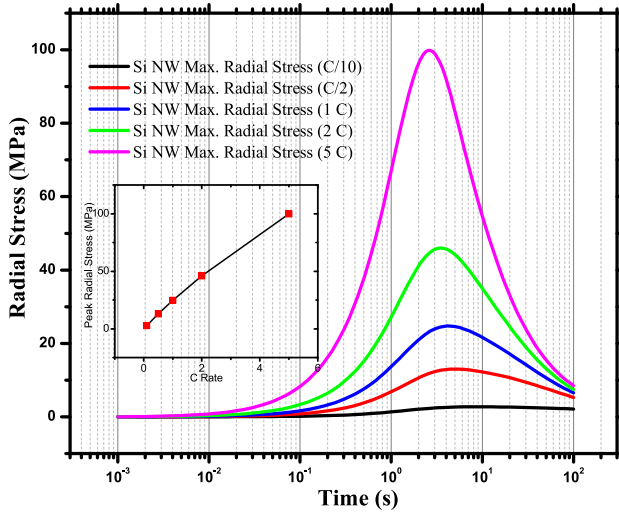


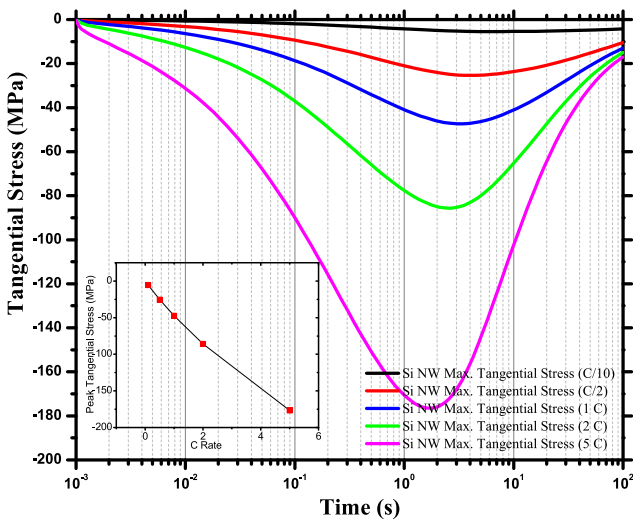
Fig. 6. Evolution of maxim radial stress ($r = 0$), maximum tangential stress ($r = R_{NW}(t)$) and maximum axial stress ($r = 0$) with time at half the height of the nanowire ($z = H_{Cu} + H_{NW}/2$). A constant 1-hr rate current equivalent to a current density (initial) of $0.0208 \text{ mA cm}^{-2}$ was used in this simulation. Plot in the subset shows the evolution of the ratio of diffusive flux and the pressure induced flux to the overall surface flux with time. A constant 1-hr rate current equivalent to a current density (initial) of $0.0208 \text{ mA cm}^{-2}$ was used in these simulations.

short times, $t = 1$ and $t = 10$ s, the stress profiles across the radius matched quantitatively with the stresses profiles across the radius in the center region of the Si NW (as discussed in the earlier section), while at longer times the presence of the constraint (substrate) significantly alters the stress profiles. At 100 s, the radial and tangential stress profiles are similar to short time behavior, however the axial stress becomes less tensile at the center and at longer times ($t = 1000$ s) the axial stress reverses its general trend and becomes compressive in the inner part and tensile at the outer part. Furthermore, the magnitude of all the stress components increases considerably and are in the range of 250–500 MPa. This is possibly because of the constant lithiation flux (imposed by the boundary conditions) in the regions close to the interface, while simultaneously the interface is also being constrained by the Cu substrate resulting in the large tensile and compressive stress regions. These enormous stress components could potentially cause the Si NW structure to yield or fracture in these regions close to the interface.

Fig. 6 shows the evolution of maximum stress for each component with time during lithiation of the Si NW. In this plot, the z co-ordinate is halfway through the initial height of Si NW, i.e. $z = H_{Cu} + H_{NW}/2$ and the r co-ordinate is chosen corresponding to where the maximum value of stress in each component occurs. The maximum radial and axial stresses are tensile and always occur at the center ($r = 0$) of the Si NW, while the maximum tangential stresses are compressive and occur at the outer surface of the Si NW, i.e. $r = R_{NW}(t)$. For the parameters used in the simulation, the values for the stress components peak at ~ 4 s and decrease subsequently. As explained in the earlier section, this behavior is due to the competing effects of the chemical diffusion term and the pressure induced term in equation (2) towards the overall flux of the species. The plot in the subset of Fig. 6 clearly shows the shift



(a) Radial stresses at the center of the Si NW, i.e. at $(z, r) = (H_{Cu} + \frac{H_{NW}}{2}, 0)$



(b) Tangential stresses at the outer radius of the Si NW, i.e. at $(z, r) = (H_{Cu} + \frac{H_{NW}}{2}, R_{NW}(t))$

Fig. 7. Evolution of stresses for different lithiation rates. 1C rate corresponds to a constant 1-hr rate current equivalent to a current density (initial) of $0.0208 \text{ mA cm}^{-2}$.

from the diffusion dominated transport at short times, to pressure driven transport at longer times.

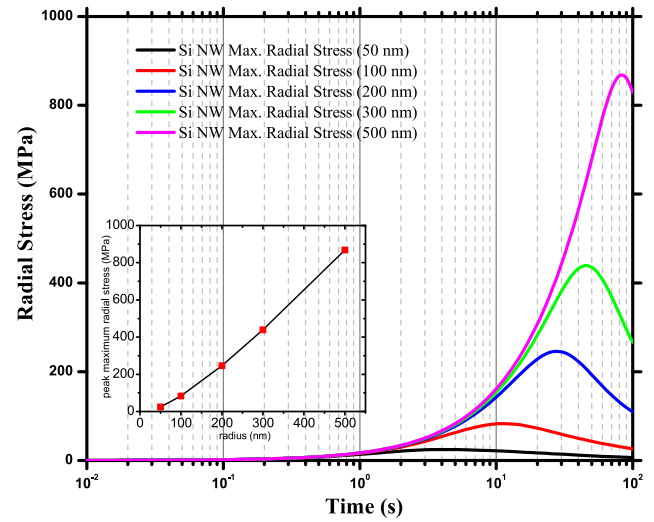
4.2. Effect of lithiation rate

Figs. 7a and b shows the effect of lithiation rate on the evolution of the maximum radial and tangential stresses with time. Here C rate corresponds to a 1-h rate equivalent to an initial current density of 0.02 mA cm^{-2} . The inset plots in Figs. 7a and b show a linear increase in maximum radial and tangential stresses with lithiation rate. Also at higher lithiation rates, the peak maximum stresses occur at shorter times as seen from the shift in the peak towards the left. This behavior suggests possibility for mechanical fracture at very short times under high current conditions, typically seen in hybrid electric vehicle, fast charge or regenerative braking applications, despite the nanoscale dimensions of the electrode. The occurrence of peak maximum stresses at shorter times at

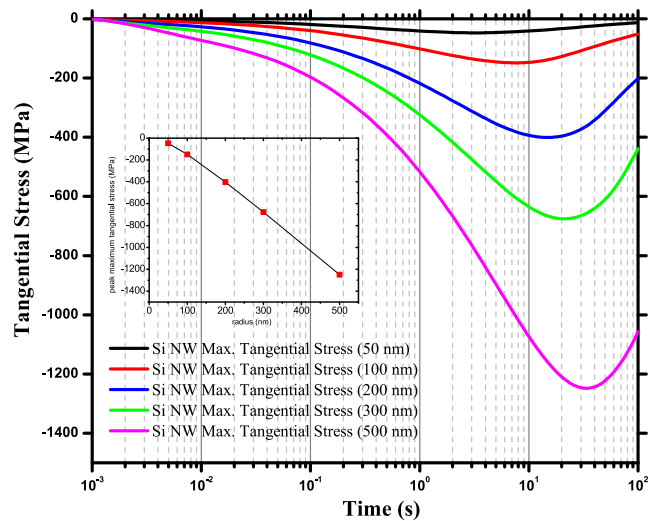
higher lithiation rates, could also be explained through the interplay between the diffusive and the pressure induced flux. At higher rates, large concentration gradients (due to chemical diffusion) are established at shorter times, creating a large stress field at the surface. Consequently, a larger pressure gradient is built up, which then dominates the species flux, compared to the chemical diffusion mode in the bulk of the Si NW.

4.3. Effect of Si NW radius

Figs. 8a and b show the effect of Si NW radius on the evolution of maximum radial and tangential stresses with time for 1-h lithiation rate. The 1-h lithiation rate (C rate) for the Si NW radii of 50, 100, 200, 300 and 500 nm corresponds to a current density of 0.0208, 0.0415 and 0.0826, 0.0826, and $0.1251 \text{ mA cm}^{-2}$ respectively. The



(a) Radial stresses at the center of the Si NW i.e. at $(z, r) = (H_{Cu} + \frac{H_{NW}}{2}, 0)$



(b) Tangential stresses at the outer radius of the Si NW, i.e. at $(z, r) = (H_{Cu} + \frac{H_{NW}}{2}, R_{NW}(t))$

Fig. 8. Evolution of stresses for different radii of Si NW at 1-hr lithiation rate. The current used in each case (C rate), corresponds to a current density (initial) equivalent to $0.0208 \text{ mA cm}^{-2}$, $0.0415 \text{ mA cm}^{-2}$, $0.0826 \text{ mA cm}^{-2}$, $0.1251 \text{ mA cm}^{-2}$, and $0.2085 \text{ mA cm}^{-2}$, for Si NW of radius 50, 100, 200, 300 and 500 nm respectively.

increased surface current density explains the higher radial and tangential stresses observed in structures with larger radii. Also, the increased current densities (for larger radius), shift the peak maximum stresses to longer times, which is contrary to the effect observed at higher current densities for constant radius (Fig. 7a and b). This behavior suggests that the increase in the current density (for larger radius structures) is not large enough to counter the longer diffusion length, which in turn delays the time for maximum stresses to develop. Consequently, the contribution from pressure induced flux takes a longer time to offset the diffusion dominated flux for nanowires with larger radii. Further, since the stress values for particles of larger radius are at any time higher than that for the particles with smaller radius, the latter is preferred especially for high rate applications. While smaller particles are not preferred due to lower compressed density and higher exposed surface area to the electrolyte, they clearly offer an advantage from a mechanical stand point. Design of optimal particle size should however be considered based on the energy and power requirements for specific applications.

5. Conclusions

A 2-d transient numerical model to simulate the electrochemical lithiation of Si NW is presented. The model predicts non-uniform volumetric strain along the length of the Si NW, with regions of maximum expansion at the top of the Si NW and almost no expansion close to the Cu CC interface. The magnitudes of the stress components are very high at the Si NW/Cu CC interface, compared to the stresses developed far away from the interface. The stress evolution with time is strongly dependent on the relative magnitudes of chemical and the pressure diffusion fluxes. The maximum stresses occur during the time when the flux is dominated by the chemical diffusion term, i.e. ~ 1 – 10 s for the rates and radius chosen for the simulations. Increase in radius of the nanowire and increase in lithiation rates develop larger radial and tangential stresses. Further, the peak maximum stresses occur at shorter times with increase in lithiation rates, while it occur at longer times with increase in the radius of the nanowire. The comparison of the results from the 2-d numerical model to the 1-d (radial) model and the evaluation of stresses for different geometries are presented in Part II of this work.

Acknowledgments

Applied Materials Inc. assisted in meeting any publication costs of this article.

Nomenclature

c	concentration of species, c_S , c_{LiS} or c_T , mol m^{-3}
N_{LiS}	flux of species c_S , or c_{LiS} $\text{mol m}^{-2} \text{s}^{-1}$
x	mole fraction of species, x_S or x_{LiS}
Δz	insertion coefficient of Li in $\text{Li}_{\Delta z}\text{Si}_{1/\Delta z}$
Δx	maximum number of moles of Li that can reversibly alloy per mole of Si
t	time, s
r	radial co-ordinate, m
θ	tangential co-ordinate, deg
z	axial co-ordinates, m
v	velocity of species, v_S or v_{LiS} , m s^{-1}
v^\diamond	molar average velocity, m s^{-1}
D_{LiS}	binary diffusion coefficient of Li in LiS, $\text{m}^2 \text{s}^{-1}$
α_{LiS}	thermodynamic factor
M	molar mass of species, M_S or M_{LiS} , g mol^{-1}
F	Faraday's constant, $\text{C g}^{-1} \text{equiv}$
R	universal gas constant, $\text{J mol}^{-1} \text{K}^{-1}$

T	temperature, K
s_i	stoichiometric coefficient
\bar{V}	partial molar volume of species LiS, \bar{V}_{LiS} or molar volume of host material S, \bar{V}_S , $\text{m}^3 \text{mol}^{-1}$
ξ	expansion factor as described in equation (5)
ρ	density of $\text{Li}_2\text{Si}_{1/\Delta x}$, g m^{-3}
p	thermodynamic pressure, N m^{-2}
\mathbf{u}	displacement vector field
u	displacement in r co-ordinate, m
v	displacement in θ co-ordinate, m
w	displacement in z co-ordinate, m
\mathbf{n}	unit outward normal vector, m
i_{app}	current density related to the outer surface area of the Si NW, A m^{-2}
R_{NW}	radius of the nanowire, also a function axial co-ordinate and time, m
H	height (z axis) of the structure, i.e. nanowire or Cu current collector
τ	stress tensor matrix
σ	stress components of the stress tensor matrix, N m^{-2}
ϵ	strain tensor matrix
ϵ	strain components of the strain tensor matrix, N m^{-2}
λ	Lame constant given by $E\nu/(1+\nu)$, N m^{-2}
μ	Lame constant given by $E/2(1+\nu)(1-2\nu)$, N m^{-2}
E	Young's modulus, N m^{-2}
K	isothermal bulk modulus given by $E/3(1-2\nu)$, N m^{-2}
ν	Poisson's ratio

Subscripts

LiS	lithiated host
S	unoccupied host
ch	chemical
T	total
max	maximum
NW	nanowire
Cu	Cu current collector

References

- [1] V.L. Chevrier, J.R. Dahn, J. Electrochem. Soc. 156 (6) (2009) A454–A458.
- [2] L.Y. Beaulieu, K.W. Eberman, R.L. Turner, L.J. Krause, J.R. Dahn, Electrochem. Solid State Lett. 4 (9) (2001) A137–A140.
- [3] M.N. Obrovac, L. Christensen, Electrochem. Solid State Lett. 7 (5) (2004) A93–A96.
- [4] C.K. Chan, H. Peng, G. Liu, K. McIlwrath, X.F. Zhang, R.A. Huggins, Y. Cui, Nat. Nano 3 (1) (2008) 31–35.
- [5] L.F. Cui, R. Ruffo, C.K. Chan, H.L. Peng, Y. Cui, Nano Lett. 9 (1) (2009) 491–495.
- [6] A. Magasinski, P. Dixon, B. Hertzberg, A. Kvit, J. Ayala, G. Yushin, Nat. Mater. 9 (4) (2010) 353–358.
- [7] M. Doyle, T.F. Fuller, J. Newman, J. Electrochem. Soc. 140 (6) (1993) 1526–1533.
- [8] M. Doyle, J. Newman, A.S. Gozdz, C.N. Schmutz, J.M. Tarascon, J. Electrochem. Soc. 143 (6) (1996) 1890–1903.
- [9] P. Ramadass, B. Haran, P.M. Gomadam, R. White, B.N. Popov, J. Electrochem. Soc. 151 (2) (2004) A196–A203.
- [10] G. Sikha, B.N. Popov, R.E. White, J. Electrochem. Soc. 151 (7) (2004) A1104–A1114.
- [11] K.E. Thomas, J. Newman, J. Electrochem. Soc. 150 (2) (2003) A176–A192.
- [12] K. Kumaresan, G. Sikha, R.E. White, J. Electrochem. Soc. 155 (2) (2008) A164–A171.
- [13] W.B. Gu, C.Y. Wang, J. Electrochem. Soc. 147 (8) (2000) 2910–2922.
- [14] S. Prussin, J. Appl. Phys. 32 (10) (1961) 1876–1881.
- [15] C. Wang, X. Cheng, A.M. Sastry, S.B. Choi, J. Eng. Mater. Technol.-Trans. ASME 121 (10) (1999) 503–513.
- [16] W.L. Wang, S. Lee, J.R. Chen, J. Appl. Phys. 91 (6) (2002) 9584–9590.
- [17] S.B. Lee, W.L. Wang, J.R. Chen, Mater. Chem. Phys. 64 (4) (2000) 123–130.
- [18] S.C. Ko, C.T. Hu, S. Lee, Y.T. Chou, Cmc-Comput. Mater. Contin. 28 (4) (2012) 165–179.
- [19] X.C. Zhang, W. Shyy, A.M. Sastry, J. Electrochem. Soc. 154 (10) (2007) A910–A916.
- [20] M.W. Verbrugge, Y.-T. Cheng, J. Electrochem. Soc. 156 (9) (2009) A927–A937.
- [21] Y.T. Cheng, M.W. Verbrugge, J. Power Sources 190 (2) (2009) 453–460.

- [22] S. Renganathan, G. Sikha, S. Santhanagopalan, R.E. White, J. Electrochem. Soc. 157 (2) (2010) A155–A163.
- [23] R. Deshpande, Y.T. Cheng, M.W. Verbrugge, J. Power Sources 195 (8) (2010) 5081–5088.
- [24] R. Deshpande, Y.T. Cheng, M.W. Verbrugge, A. Timmons, J. Electrochem. Soc. 158 (6) (2011) A718–A724.
- [25] M. Zhu, J. Park, A.M. Sastry, J. Electrochem. Soc. 159 (4) (2012) A492–A498.
- [26] J. Christensen, J. Newman, J. Solid State Electrochem. 10 (5) (2006) 293–319.
- [27] J. Christensen, J. Newman, J. Electrochem. Soc. 153 (6) (2006) A1019–A1030.
- [28] J. Christensen, J. Electrochem. Soc. 157 (3) (2010) A366–A380.
- [29] R. Chandrasekaran, A. Magasinski, G. Yushin, T.F. Fuller, J. Electrochem. Soc. 157 (10) (2010) A1139–A1151.
- [30] R. Chandrasekaran, T.F. Fuller, J. Electrochem. Soc. 158 (8) (2011) A859–A871.
- [31] Y.F. Gao, M. Zhou, J. Appl. Phys. 109 (1) (2011) 014310.
- [32] C.J. Wen, R.A. Huggins, J. Solid State Chem. 37 (3) (1981) 271–278.
- [33] M.N. Obrovac, L. Christensen, D.B. Le, J.R. Dahn, J. Electrochem. Soc. 154 (9) (2007) A849–A855.
- [34] P. Limthongkul, Y.I. Jang, N.J. Dudney, Y.M. Chiang, Acta Mater. 51 (2) (2003) 1103–1113.
- [35] D. Larcher, S. Beattie, M. Morcrette, K. Edstroem, J.C. Jumas, J.M. Tarascon, J. Mater. Chem. 17 (36) (2007) 3759–3772.
- [36] J.C. Slattery, Advanced Transport Phenomena, Cambridge [u.a.]: Cambridge Univ. Press, 1999.